PAPER

Highly stable nano Ce–La catalyst for hydrogen production from bio-ethanol

Dalia R. Abd El-Hafiz, Mohamed A. Ebiad,* Radwa A. Elsalamony and Lamia. S. Mohamed

The catalytic activity of a metal free nano particle, whose size ranged from 1–10 nm, was studied according to HRTEM and DLS results. The effect of reaction temperature (300–600 °C) on the catalytic activity of the prepared catalysts was studied in a flow system under atmospheric pressure with an ethanol–water molar ratio of 1 : 10. Selectivity was calculated for the products H_2, CO, CO_2 and CH_4, as well as the intermediates C_2H_6, C_2H_4, CH_3CHO and CH_3COCH_3, at different reaction temperatures. It was found that the addition of La increased the activity and stability of the Ce catalyst. H_2 was produced at the lowest temperature (300 °C) over Ce–La$_{0.2}$ & Ce–La$_{0.5}$ catalysts. Complete conversion of ethanol with high hydrogen selectivity was obtained at 500 °C over Ce–La$_{0.2}$ catalysts. Further increases of La content lead to decrease in the catalyst activity in accordance with the decrease of surface area to 9.6 m^2 g^{-1}. To study the stability of the prepared catalyst, the ESR reactions of Ce–La$_{0.2}$ and Ce–La$_1$ catalysts were investigated at 500 °C for 15 h. It was found that the Ce–La$_{0.2}$ catalyst is more stable than the Ce–La$_1$ catalyst over entire 15 h. Finally, we can say that lanthanum oxide (La_2O_3) is particularly suitable as a modifier due to its effectiveness in the prevention of sintering and improvement of thermal resistance at high temperatures. This oxide is also able to gasify the coke through the formation of $La_2O_2CO_3$ oxy-carbonate.

1. Introduction

The reduction of greenhouse gas emissions from the exhaust of vehicles is one of the most important challenges, and it has recently attracted increasing attention. Hydrogen vehicles will provide higher vehicle efficiency along with significant reductions in emissions.[1–3] Thus, hydrogen is a promising alternative fuel and has been an energy carrier for decades; it has been used for the generation of electricity in fuel cells and as fuel for transportation without CO_2 emissions. Currently, the production of hydrogen is mainly obtained from fossil fuels:[4,5] 48% from natural gas, 30% from oil-derived naphtha and 18% from coal, which results in the co-production of CO_2. The future hydrogen market requires its production to be performed in a sustainable way from renewable raw materials. Thus, numerous researchers[4,6–11] have studied the catalytic reforming of bio-ethanol as a way to replace fossil fuels.

Steam reforming of bio-ethanol ($C_2H_5OH + 3H_2O \rightarrow 6H_2 + 2CO_2$) over supported metal oxide leads to high H_2 yields at reasonable costs.[12] However, the endothermic nature of this reaction ($\Delta H^{\circ}_{298\ K} = 174.4$ kJ mol^{-1}) requires high temperatures (700–1000 K) to achieve good ethanol conversion. This high temperature favors the reverse water–gas shift reaction ($CO_2 + H_2 \rightarrow 4CO + H_2O$) and thus generates CO, which degrades the

performance of Pt electrodes in fuel cell systems.[13,14] Moreover, steam reforming is a complex reaction and several side reactions can take place, forming undesired by-products (such as acetaldehyde, ethylene, methane and acetone)[4] that lower the overall H_2 yield and can get converted to coke deposits, resulting in catalyst deactivation.[15] Therefore, reducing the undesired byproducts is a very important issue in low-temperature hydrogen production.

Accordingly, the major challenge in steam reforming of bio-ethanol is the use of appropriate catalysts. Several types of supported transition and noble metals have been studied as active and selective catalysts in the ESR system, but improvement of their stability is required due to sintering and carbon deposition.[16,17] Despite its widespread applications, the use of pure cerium dioxide is highly discouraged because its thermal stability is poor because it undergoes sintering at high temperatures, thus losing its crucial oxygen storage and release characteristics. The modification of ceria with other metals, like Zr^{4+}, Hf^{4+}, Ti^{4+}, and La^{3+}, is a key issue to overcome the aforesaid drawbacks. Lanthanum oxide (La_2O_3) is particularly suitable as a modifier due to its effectiveness in preventing sintering and improving thermal resistance at high temperatures.[18,19] This oxide is also able to gasify the coke through the formation of $La_2O_2CO_3$ oxy-carbonate species.

Ceria nano-particles are synthesized by various aqueous solution methods such as hydrothermal synthesis,[20] precipitation,[21] forced hydrolysis,[22] and electrochemical synthesis.[23]

Egyptian Petroleum Research Institute, Cairo, 11727, Egypt. E-mail: m_a_ebaad@yahoo.com; Fax: +20 222747433; Tel: +20 01274445773

However, ceria nano-particles prepared by aqueous solution methods exhibit hard agglomeration between adjacent particles due to hydrogen bonds and a huge capillary force during drying.[24] Freeze-drying technology is an advanced technology for metal oxide preparation; it imparts two main advantages: it endows materials with higher surface area and improves the uniformity of distribution.[25] The process is simple to operate, and it has been used in the preparation of ultra-fine metal powders (*i.e.*, it is easy to control the nucleation),[26] and catalytic materials.[27] Xiaoli Xi,[28] in her earlier research, used this method to prepare a series of nano rare-earth tungsten powders (W–La₂O₃, W–Y₂O₃, W–CeO₂) and nickel powders.[29–31] By spraying a solution or a powder suspension into liquid nitrogen, the drops (granules) were instantaneously frozen. In a subsequent freeze-drying cycle, the granules were dried by the sublimation of the ice without any segregation effects, as in the case of conventional drying in the air. The process resulted in the formation of spherical and free flowing granules with optimal homogeneity.

Thus, in this work, a smart ultra-fine Ce–La$_x$ catalyst prepared by the spray freeze-drying method, without metal addition, was used in ethanol steam reforming reaction to produce hydrogen. Three $CeO_2La_xO_{1.5}$ solid solutions were prepared with different La content (x = 0.2, 0.5 and 1). The prepared catalysts were investigated using XRD, TGA, BET surface area, DLS techniques and HRTEM. The catalysts were tested in a bio-ethanol steam reforming reaction, to observe increase in ethanol conversion and hydrogen yield and decrease in CO by-product and coke deposition.

2. Experimental

2.1. Catalyst preparation

Three Ce–La$_x$ (x = 0.2, 0.5 and 1) solid solution catalysts were prepared by the spray freeze-drying method. Fig. 1 shows the schematic diagram of the main procedure of the method, which mainly involves three steps: freeze granulation, vacuum drying and heat treatment.

Using Cerium nitrate ($Ce(NO_3)_2 \cdot 6H_2O$, 99% Fluka) and lanthanum nitrate ($La(NO_3)_3 \cdot 6H_2O$, 99% Cambrian Chemicals) as a precursor, three solutions containing 0.05 M ceria with different lanthanum molar ratios (Ce : La = 1 : 0.2, 1 : 0.5, and 1 : 1) were prepared. The solutions were dispersed in liquid

nitrogen through an airbrush, using air as a carrier. Then, the frozen droplets were placed under vacuum for about 36 h. Finally, the catalysts were calcined in air flow at 500 °C for 4 h.

2.2. Catalyst characterization

Thermal gravimetric analysis (TGA). Thermal gravimetric analysis (TGA) was carried out using a SETARAM Labsys TG-DSC16 equipment in the temperature range from room temperature to 1000 °C under a nitrogen flow to follow the thermal stability of the prepared catalyst.

X-ray diffraction analysis (XRD). X-ray Diffraction Analysis (XRD) was carried out by a Shimadzu XD-1 diffractometer using a Cu-target and Ni-filtered radiation to trace the various changes in the crystalline structure and the different phases that occur during preparation. The sample powders were packed in a glass holder during the measurement of the diffraction intensity with a step scanning in the 2θ range between 4° and 90°. The phase identification was made by comparing the results with the Joint Committee on Powder Diffraction Standards (JCPDS). The crystalline size, D_{XRD}, was calculated according to the Scherrer equation: $D_{XRD} = 0.9\lambda/B \cos \theta$, where λ is the wavelength of the radiation, and θ is the diffraction angle. B is the corrected half-width of the diffraction peak. The reflection from the (111) plane was used to calculate the crystallite size. The geometrical specific surface area (S_{XRD}) was also determined, assuming spherical particles, according to the equation $S_{XRD} = 6 \times 10^3/\rho D_{XRD}$, where ρ (g cm^{-3}) is the theoretical density. Scherrer analysis was performed to determine the average crystalline domain size, which was calculated by the Scherrer formula ($D = 0.89\lambda/\beta \cos \theta$) with the FWHM and a peak position (2θ) of several peaks, where D is the crystallite size, λ is the wavelength of the radiation, β is the corrected peak width at half-maximum intensity, and θ is the peak position. The average value is given as the mean crystallite size.

Temperature programmed reduction (TPR). Temperature programmed reduction (TPR) measurements were carried out to investigate the redox properties (the ease of reducibility of the metal oxide) over the resultant materials. The experiments were performed in automatic equipment (ChemBET 3000, Quantachrome). Typically, 100 mg of a pre-calcined sample was loaded into a quartz reactor and pretreated by heating under an inert atmosphere (20 ml min^{-1} nitrogen) at 200 °C for 3 h prior to running the TPR experiment, and then it was cooled to room temperature in N₂. Then, the sample was subjected to a constant rate of heat treatment (10 °C min^{-1} to 1000 °C) in a gas flow (80 ml min^{-1}) of a hydrogen/nitrogen (5/95 vol%) mixture as the reducing gas. A thermal conductivity detector (TCD) was employed to monitor the amount of hydrogen consumption.

High resolution transmission electron microscopy (HRTEM) and energy dispersive X-ray (EDS). High resolution transmission electron microscopy (HRTEM) and energy dispersive X-ray (EDS) spectroscopy were conducted using a JEOL 2100F TEM at an accelerating voltage of 200 kV. To prepare the TEM samples, a dilute particle–ethanol colloidal mixture was ultra-sonicated for 30 min and a drop of the solution was placed on a carbon coated Cu TEM grid.
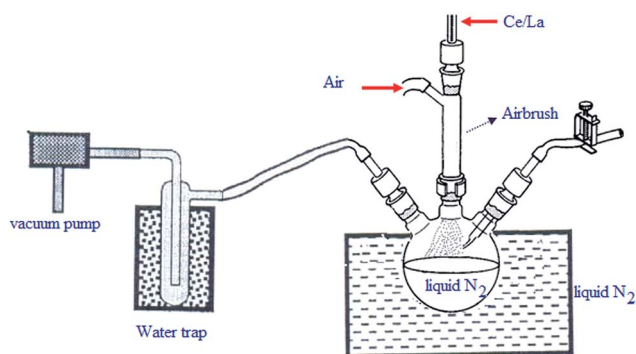

Fig. 1 Spray freeze-drying method.

The textural properties. The textural properties were determined from the N_2 adsorption–desorption isotherms measured at the liquid nitrogen temperature ($-196\ °C$) using a NOVA2000 gas sorption analyzer (Quanta Chrome Corporation) system. All the samples were degassed at $200\ °C$ for 17 h in nitrogen atmosphere prior to adsorption to ensure a dry and clean surface. The adsorption isotherm was constructed as the volume adsorbed ($V\ cm^3\ g^{-1}$) versus the equilibrium relative pressure P/P_o, where P is the equilibrium pressure and P_o is the saturated vapor pressure of nitrogen. The BET surface area (S_{BET}) was calculated using the five-point Brunauer–Emmett–Teller (BET) theory. Mean particle size (D_{BET}) was calculated from the BET data according to $D_{BET} = 6/(\rho S_{BET})$.

2.3. Catalytic activity

Bio-ethanol steam reactions were carried out at atmospheric pressure in a continuous flow system consisting of a fixed-bed tubular reactor (schematically represented in Fig. 2). 0.5 g of catalyst (size: 50–80 mesh) diluted with 0.5 g of same sized quartz particles were used for catalytic tests. Prior to a run, the catalyst was in situ reduced at $500\ °C$ for 2 h under a hydrogen flow rate of $40\ cm^3\ min^{-1}$. A water–ethanol mixture ($EtOH–H_2O = 1:10$ mol/mol) premixed in a separate container was fed into a pre-heater made in a SS316 reactor (at $150\ °C$) by a dosing pump (Model RP-G6; FMI, USA) with a flow rate of $0.1\ ml\ min^{-1}$. Nitrogen was used as the carrier gas with a flow rate of $40\ cm^3\ min^{-1}$. The reaction temperature was varied from 300 to $600\ °C$. The product stream was analyzed by two gas chromatographs (GC) (Agilent 6890 plus HP, Varian Natural Gas Analyzer type C model CP-3800). The conversion and selectivity to products formed during the reaction were calculated according to a previous report.[32]

3. Results and discussion

3.1. Catalyst characterization

Energy dispersive X-ray spectroscopy (EDX). Energy dispersive X-ray spectroscopy (EDX) pattern (Fig. 3) shows that there
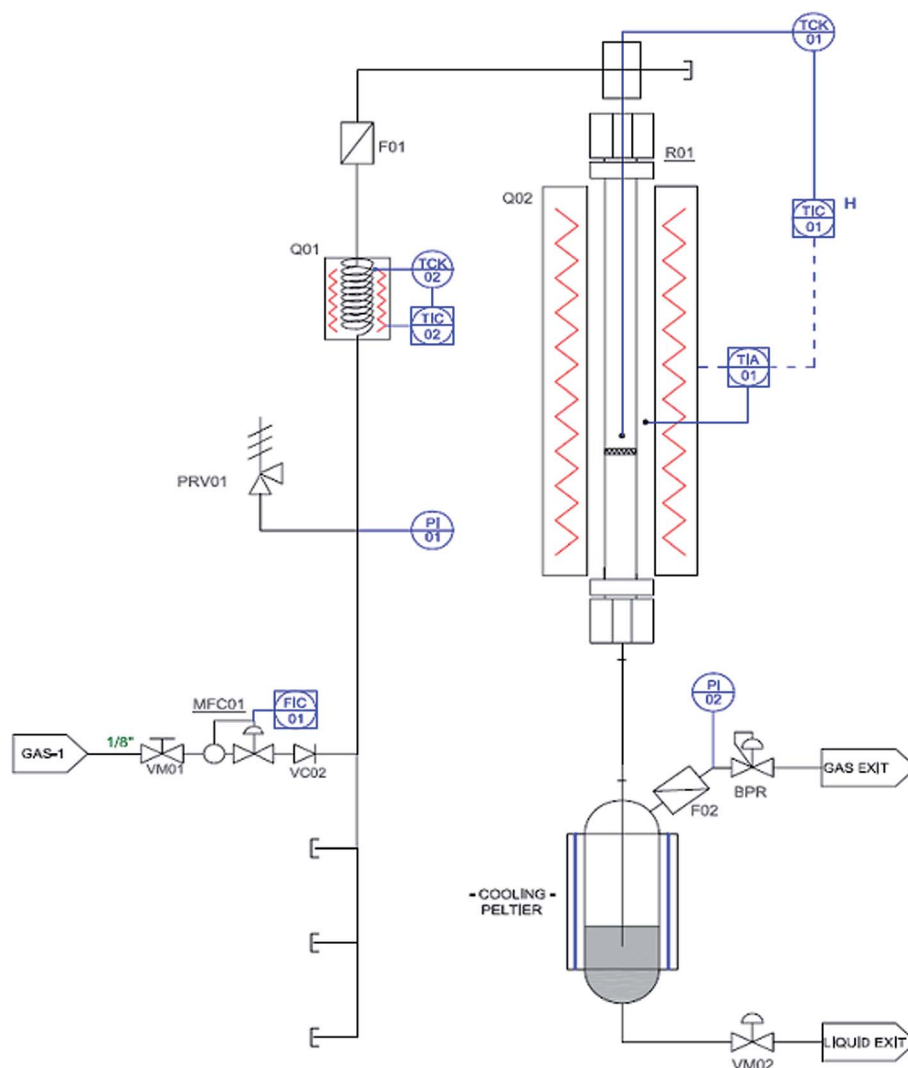

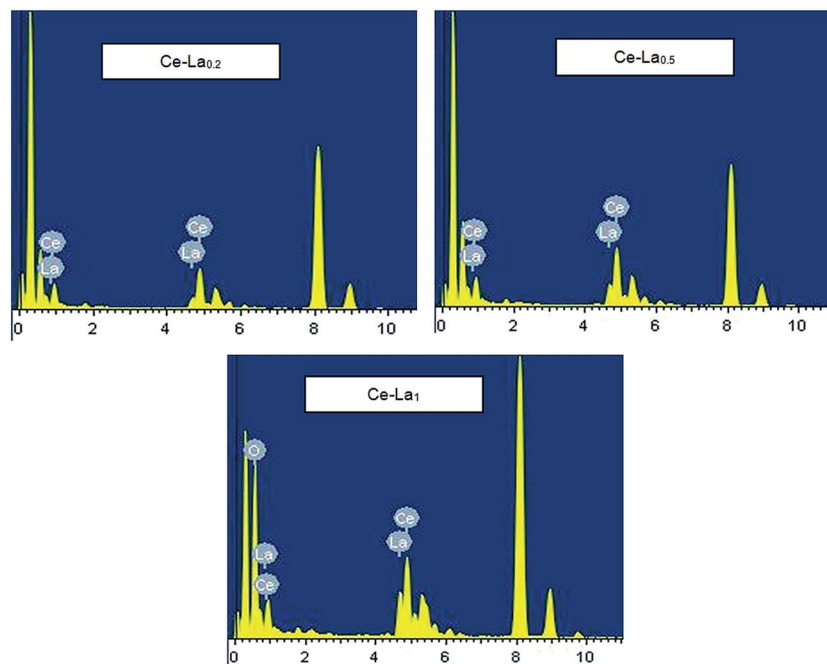Fig. 2 Schematic diagram of a catalytic flow system.

Fig. 3 EDX pattern of the prepared Ce–La catalysts.

are peaks at about 1.1 and 4.8 keV corresponding to Ce and others around 0.8 and 4.6 keV corresponding to La. As stated before, $CeO_2-La_xO_{1.5}$ oxides were prepared by a spray freeze drying method with different Ce : La molar ratios (where, $x = 0$, 0.2, 0.5 and 1). From Table 1, it can be found that a mean atomic ratio was obtained in excellent agreement with the nominal composition used in the synthesis. It is worth noting that EDX shows the elemental analysis of one surface point only; thus, the average results of five points were tested, and they are shown in Table 1.

Thermal gravimetric analysis (TGA). Thermal gravimetric analysis (TGA) of the dried samples was performed to determine the correct calcination temperature. The TGA profiles (Fig. 4) of the prepared Ce–La$_x$ catalysts from room temperature to 1000 °C show two steps weight loss: a first decrease at 100 °C due to the adsorbed water on powder, and then a smaller decreasing step at 350 °C. The total weight losses were 25.27%, 32.08% and 43.77% for Ce–La$_{0.2}$, Ce–La$_{0.5}$ and Ce–La$_1$, respectively. The weight loss and the corresponding endothermic reactions suggested the decomposition reactions of the compound or mixture. Moreover, the small exothermic peak
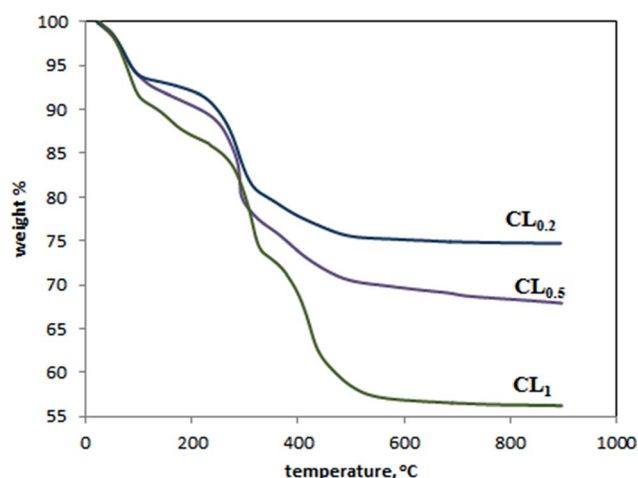

Fig. 4 TGA profiles of the prepared samples.

detected at 300 °C may be due to a crystallization phenomenon and due to the formation of a Ce–La solid solution.[33] The decomposition was complete at 500 °C; thus, all the samples were calcined at this temperature.

X-ray diffraction (XRD). X-ray diffraction (XRD) was used to determine the nature of the phases present in Ce–La$_x$ (Ce : La atomic ratio 1 : 0, 1 : 0.2, 1 : 0.5 and 1 : 1) samples (Fig. 5). For all the catalysts, peaks were detected corresponding to the typical face centered cubic (FCC) fluorite structure of CeO_2 (JCPDS 00-002-1306).[34] The (111) plane for CeO_2 fluorite structure (28.507° in CeO_2) shifted to lower angles as the La content increased (28.31°, 28.09° and 27.4° for Ce–La$_{0.2}$, Ce–La$_{0.5}$ and Ce–La$_1$, respectively), which is also reflected by an increase in

Table 1 Ce : La atomic ratio

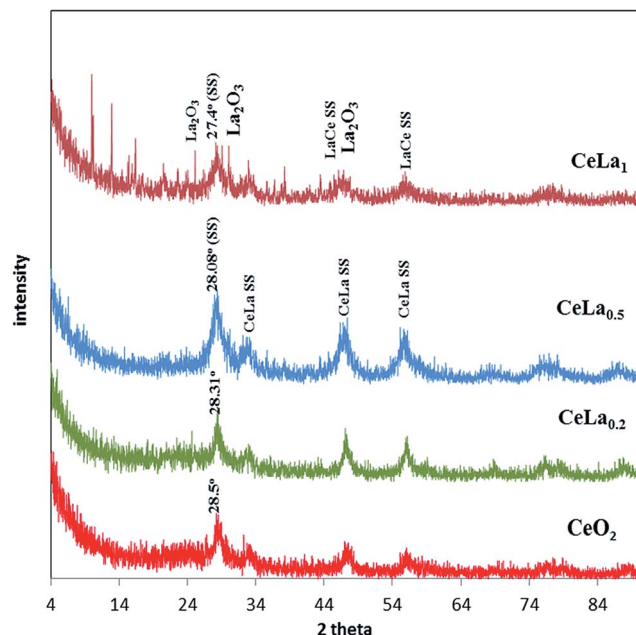| Element	Atomic%		
	Ce–La$_{0.2}$	Ce–La$_{0.5}$	Ce–La$_1$
La	6.3	12.8	19.6
Ce	33.7	27.2	20.4
O	60	60	60
La/Ce atomic ratio	0.188	0.471	0.965

Fig. 5 XRD patterns of CeO_2 and $CeO_2La_xO_{1.5}$ catalysts.

the lattice parameter "a", as reported in Table 1. This shift can be explained as the lattice expansion of CeO_2 and the formation of ceria lanthanum solid solutions due to the larger radius of La^{3+} (1.10 Å) *versus* Ce^{4+} (0.97 Å).[6] This is an indication of the increasing number of oxygen vacancies as the La doping increases.[35] Moreover, no second phases or additional reflections were found in $Ce–La_{0.2}$ and $Ce–La_{0.5}$ catalysts, indicating the formation of a single phase (solid solution). However, in the case of $Ce–La_1$ catalyst, other lines were observed at 2θ = 30.064°, 26.111° and 46.28° (JCPDS 00-002-0688) due to the hexagonal phase of La_2O_3.

The XRD peaks for all the samples are considerably broad, indicating that the samples prepared by spray freezing method are in the nano-size range.[36] The average crystallite sizes determined by applying the Scherrer equation to the characteristic (111) peak of CeO_2 from the XRD results after structure refinement are listed in Table 2. In comparison to the pure ceria, which had a crystalline size of 11 nm, Ce–La had larger crystallite sizes that increased along with the La content.

An interesting observation noted from the XRD measurements was that when we calculated the lattice parameter of the (101) peak (representing the La_2O_3 phase) that appeared in Ce–La$_1$ catalyst, it was found to be 0.42 nm, which is larger than

that of the pure La_2O_3 phase. This may refer to the incorporation of Ce^{4+} (0.97) cations into the La^{3+} (1.10 Å) cations to form a La–CeO_2 solid solution in a hexagonal phase structure (larger particle size). Wilkes *et al.*[37] reported that in $Ce_{1−x}La_xO_{2−x/2}$ oxides system, at a low ionic fraction of lanthanum ($0 < x < 0.5$), lanthanum dissolved in ceria with lanthanum segregation occurring on its surface; however, at a high lanthanum content ($x > 0.9$), cerium dissolved in lanthanum with ceria segregation can be predicted.[38] In addition, the calculation of the d/D_{XRD} ratio (degree of agglomeration of the primary crystallites) indicates that the La ratio <1 decreases the particle agglomeration (d/D_{XRD}). However, when a high La ratio increases, the particle agglomeration also increases.

Temperature programmed reduction (TPR). Temperature programmed reduction (TPR) of the prepared catalysts shows a reduction profile with the occurrence of two peaks, the smaller one is an intense peak located at a higher temperature (600 °C) due to the bulk reduction of CeO_2. The H_2 uptake at this temperature was decreased by increasing amount of lanthanum due to the quantities of ceria, and thus the number of its oxygen vacancies gradually decreased. The second one is a high intense peak located at a lower temperature (512 °C) due to surface reduction.

The doping of ceria with lower valence La^{3+} leads to the introduction of oxygen vacancies that can be expressed by the Kröger–Vink notation as follows:

$$La_2O_3 \xrightarrow{2CeO_2} 2La'_{Ce} + 3O_o^x + V_o^{\cdot\cdot}$$
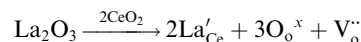
where La'_{Ce} represents the Ce^{4+} site occupied by La^{3+}. As reported by Zhang *et al.*,[39] the increase in the addition of La_2O_3 into the CeO_2 system would lead to the formation of more oxygen vacancies due to the charge compensation in the material. The vacancies ($V_o^{\cdot\cdot}$) with positive charge may attract the doping ions (La'_{Ce}) with negative charge to produce complexes ($2La'_{Ce}V_o''/2\ La'_{Ce}V_o''La'$) due to electrostatic attractions. In accordance, as the La concentration increases, the peak at 512 °C shifts to higher temperatures due to the increase in the interaction between Ce and La because at low concentrations the $V_o^{\cdot\cdot}$ are probably free and easily reducible, while at a high level of doping, the defects association near the dopants begin to form.[40]

Moreover, Fig. 6 shows that the lower temperature peak (512 °C) is accompanied by a shoulder at about 450 °C, which can be ascribed to the surface oxygen adsorbed on the Ce^{4+} vacancies produced due to the replacement of Ce^{4+} by smaller valence La^{3+}. Further increase in the dopant addition (0.5 and 1)

Table 2 XRD data of the prepared samples

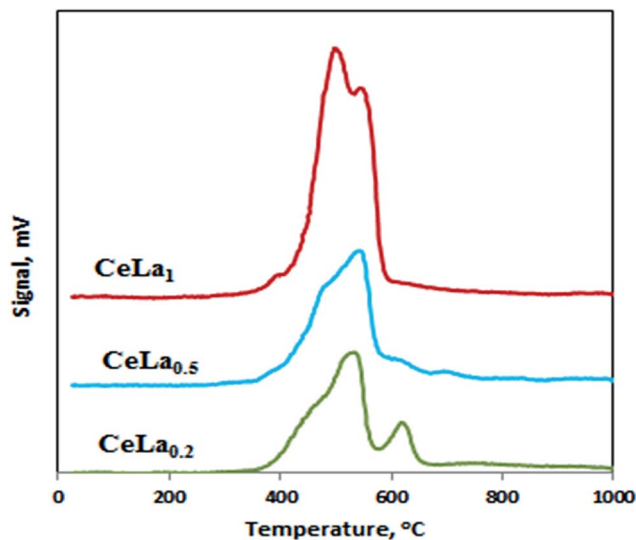|	Phase	D_{XRD} nm	a nm	S_{XRD} m^2 g^{-1}	D_{BET} nm	d/D_{XRD}
CeO_2	(111) fluorite	11.4	0.542	367	47	0.42
$Ce–La_{0.2}$		17.1	0.543	211	49	0.29
$Ce–La_{0.5}$		18.7	0.545	162	41	0.22
$Ce–La_1$	(111) fluorite	19.3	0.554	130	257	1.35
	(101) hexagonal La_2O_3	41.3	0.420			

Fig. 6 H_2 consumption profiles during TPR of $CeO_2La_xO_{1.5}$ catalysts.

causes an increase in the intensity of this shoulder (which becomes a peak at 500 °C with a shoulder at 530 °C in the case of Ce–La$_1$). The presence of this new peak at a lower temperature (500 °C) can confirm a higher Ce^{4+} replacement by La^{3+} ions, which promotes the diffusion of O^{2-} anions within the lattice, facilitating the bulk and surface reduction at lower temperatures.[41]

It can be observed from the XRD analysis that the expansion of CeO_2 lattice due to La^{3+} doping lead to lattice strain and formation of free volume, which can facilitate the equilibrium of oxygen atoms between the surface and bulk, promoting the surface-bulk oxygen transport. This phenomenon is responsible for the observed reduction behavior.[17]

Texture properties (BET). Specific surface area, pore volume and average pore diameter play an important role in the performance of the catalysts, especially in the high space velocity catalytic reaction. Thus, the catalysts must have properties, such as a large specific surface area, pore volume and a suitable pore diameter. Significant information about the textural properties of the Ce–La solid solution catalysts were obtained by the analyses of nitrogen adsorption–desorption isotherms, which are collected in Table 3.

Fig. 7 shows that all the samples show a type II isotherm according to the Brunauer classification, indicating that the adsorption proceeds by an unrestricted monolayer-multilayer adsorption on micropores. The inflection point or knee of the

isotherm indicates the stage at which the monolayer coverage is complete, followed by a multilayer adsorption. The first part of the isotherm is very pronounced, and consequently the materials present micro-porosity, as confirmed by t-plot analysis (Fig. 8). The intercept of the t-plot is almost zero for each sample and the surface area are comparable to that of the BET surface area due to the micro-pores, which may indicate that the surface area of all the samples are micro-porous. All the samples (except Ce–La$_1$ sample) exhibit closed hysteresis loops with varying closure pressures depending on the Ce : La ratio. The occurrence of a hysteresis loop in type II isotherms has been observed with the samples having parallel plate pores. However, the Ce–La$_1$ sample (Fig. 7) shows type II without hysteresis loop, *i.e.*, desorption points lie on the same adsorption isotherm. This may indicate either a nonporous structure or the meso-porosity of the entire texture. This was also confirmed by a v–t plot (Fig. 8), whose data is collected in Table 3.

Table 3 depicts the physical properties of catalysts. It shows that surface area, pore volume and pore radius decrease by the incorporation of a trivalent cation (La^{3+}) into the CeO_2 lattice, which may be attributed to the incorporation of lanthanum into the pore systems, although it may not block the pores. This was also confirmed by the BJH pore size distribution (Fig. 9), which shifted to a lower pore diameter as the La content increased. The decrease of surface area can be confirmed by the increase of the crystallite size, as shown from the XRD data. These results are nearly similar to those recently reported by Petallidou and Efstathiou.[42]

The geometrical surface areas (S_{XRD}) of the prepared oxides calculated from the XRD data are considerably higher than that obtained from the BET analysis (Table 3). This variation can be related to the fact that S_{XRD} is calculated based on the diffraction peaks of crystallites with the initial Ce–La solid solution composition, whereas S_{BET} corresponded to all the particles in the sample.[43] Furthermore, solid solutions may contain small agglomerates and grain boundary interfaces, which are not available to N_2 gas during the BET analysis. We also believe that some internal porosity associated with the grain boundary regions have an influence on the obtained results.

Dynamic light scattering (DLS). Fig. 10 shows the particle size distribution measured for Ce–La$_x$ with different Ce : La ratio. The obtained results indicate that the spray freezing method obtains catalysts with particle sizes in the nano-scale (ranged 18–50 nm), and the distribution of the powders was well-proportioned, except in the case of Ce–La$_1$.

In the process of spray freezing,[28] the droplets were sprayed into liquid nitrogen (−196 °C). Due to the rapid cooling rate, the

Table 3 Textural properties of the prepared catalysts

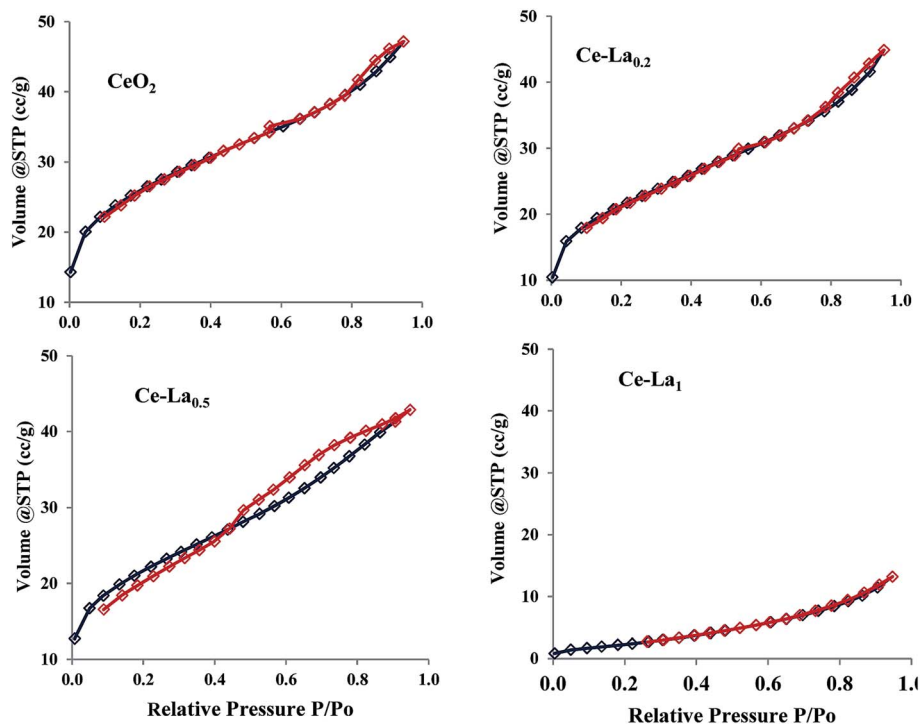|	S_{BET} m^2 g^{-1}	S_{XRD} m^2 g^{-1}	V_P cm^3 g^{-1}	r_P Å	V_{Micro} cm^3 g^{-1}	r_{Micro} m^2 g^{-1}	$S_{Ex.}$ area m^2 g^{-1}
CeO_2	87.8	367	0.086	23.91	0.025	52.59	35.2
Ce–La$_{0.2}$	74.7	211	0.084	18.45	0.017	36.93	36.7
Ce–La$_{0.5}$	72.3	162	0.062	18.50	0.019	38.27	36.0
Ce–La$_1$	9.6	130	0.030	11.38	0.000	0.00	9.6

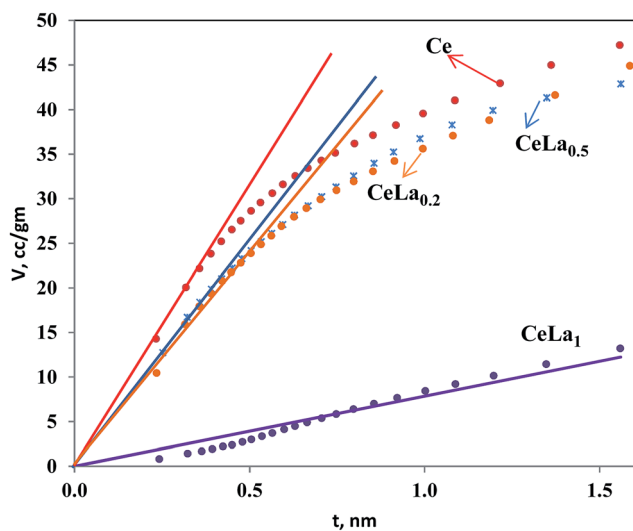Fig. 7 N$_2$ adsorption–desorption isotherms of the prepared catalysts.
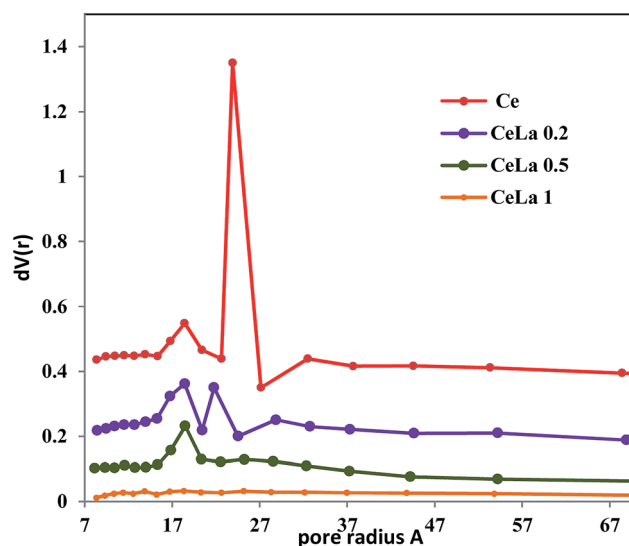

Fig. 8 t–v Plot of the prepared catalysts.

Fig. 9 Pore size distribution of the prepared catalysts.

chances of nucleation were greatly improved but the growth rate decreased, resulting in the solute precipitating in the form of ultrafine grained salts. During the rise of temperature (the process when the frozen droplets were taken out of the liquid nitrogen before the first step of freeze drying), the crystal transformation of ice (ice sublimation) resulted in some aggregation of ultrafine grained salts. When the ice sublimated, the ultra-fine grain salts turned into precursors, confirming the broad particle size distribution of all the samples.

The incorporation of La onto CeO$_2$ lattice led to an increase in the particle size distribution due to the high atomic radius of

La^{3+}, as indicated by the XRD data. Moreover it is noticeable that high concentration of La in Ce–La$_1$ allows some desegregation of the material showing a non-uniform particle size distribution pattern. This data were also confirmed by XRD.

TEM technique. TEM images obtained visual impressions of the morphology of the catalysts prepared by the spray freeze-drying method (Fig. 11 and 12). Fig. 11 indicates that the overall particle shape was non-spherical and appeared slightly aggregated for cerium oxide. The non-spherical shape of
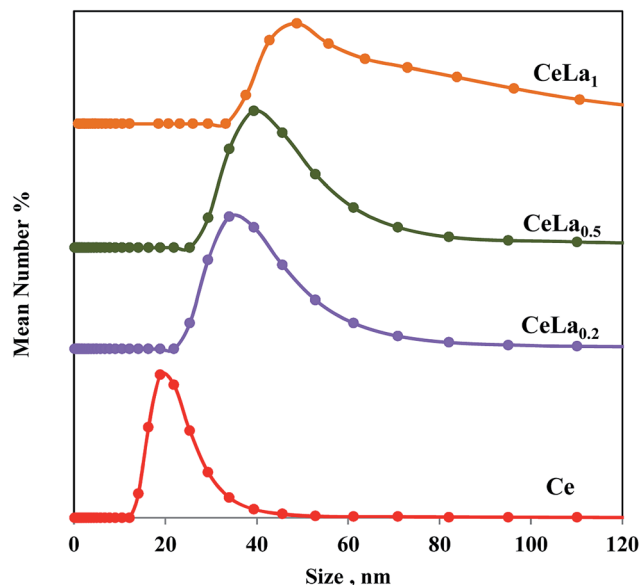
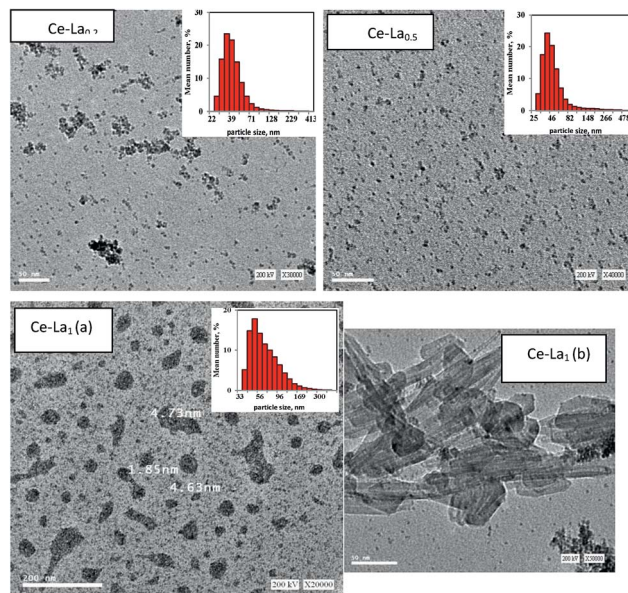Fig. 10 Particle size distribution of the prepared catalysts.

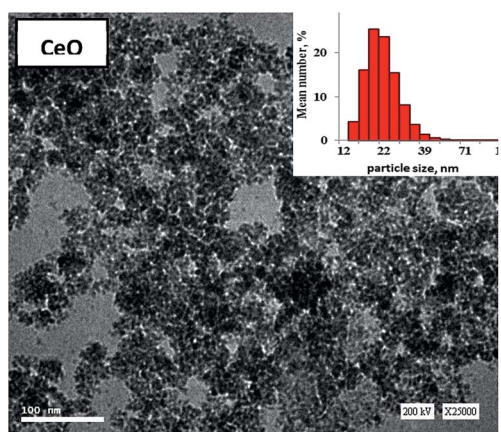Fig. 12 HRTEM images of the $CeO_2La_xO_{1.5}$ samples.

Fig. 11 HRTEM image of the CeO_2 sample.

particles for the coarse mode may be due to the fact that the particles consisting of a single crystal or a large number of crystals tend to be spheroidal.[44]

The incorporation of La^{3+} (Ce : La atomic ratio = 1 : 0.2 and 1 : 0.5) led to an increase in particle size and a decrease in the degree of agglomeration, as clearly shown by Fig. 12. However, $CeO_2La_1O_{1.5}$ exhibits very large particle size with a high degree of agglomeration (Fig. 12a). More magnified images of this sample (Fig. 12b) show the formation of Ce–La nanotube, with tube length ranging from 50 to 100 nm and a uniformly distributed diameter around 3 nm. These data agree well with the XRD and DLS data.

Catalytic activity. Fig. 13 reports the bio-ethanol conversion and hydrogen selectivity during ESR over the prepared Ce–La$_x$ catalysts with different Ce : La atomic ratio as a function of the reaction temperature. Generally, it is important to note that the low gas production (small gas yield), as shown in Fig. 14, can be attributed to the injection of small ethanol concentrations (see

Experimental section). As seen from Fig. 14, 92% of ethanol conversion with 27% hydrogen selectivity was obtained at a very low temperature (300 °C) in the presence of a Ce–La$_{0.2}$ catalyst; this percentage increases by increasing reaction temperature, until it approaches a 100% conversion with 75% H_2 (at 600 °C) over the same catalyst. Moreover, an increase in the La content leads to a decrease of both ethanol conversion and hydrogen selectivity. This can be related to the increase of the particle size, decrease in the BET surface area and increase of OSC by the increase of La content, as shown by the catalyst characterization.

Fig. 14 shows the product distribution during ethanol steam reforming over the prepared Ce–La$_x$ solid solution. From this figure, we can see that the mechanism of ESR over those catalysts contain a small amount of La that is completely different from the catalyst containing high amounts of La. In the case of Ce–La$_{0.2}$ and Ce–La$_{0.5}$ catalysts, the main reaction products were H_2 and CO_2. The trace amounts of CO, acetaldehyde, ethylene, CH_4 and acetone (less than 10%) were also produced. By increasing the reaction temperature, the selectivity to H_2 increased and the selectivity to CO_2 passed through a maximum. The selectivity to CO and CH_4 were slightly increased, while the selectivities to ethylene, acetaldehyde and acetone formation were negligible. However, in the case of the Ce–La$_1$ catalyst, the main reaction products were CO_2, acetaldehyde and acetone at lower reaction temperatures, while at higher reaction temperatures, the main products were CO_2, H_2 and CH_4. This may be attributed to the differences in the structure and morphology of Ce–La$_1$, as shown from the characterization data.

It is worth noting that the selectivity to CO over all the prepared catalysts was lower than 2%, especially at lower reaction temperatures over Ce–La$_{0.2}$ and Ce–La$_{0.5}$ catalysts, which means that these catalysts can be directly used for fuel cell application.[45]
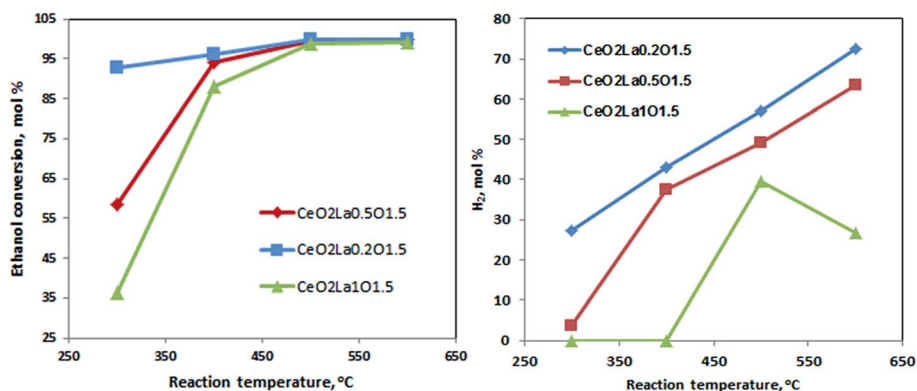
Fig. 13 Ethanol conversion and hydrogen selectivity during ESR over Ce–La$_x$ catalysts.
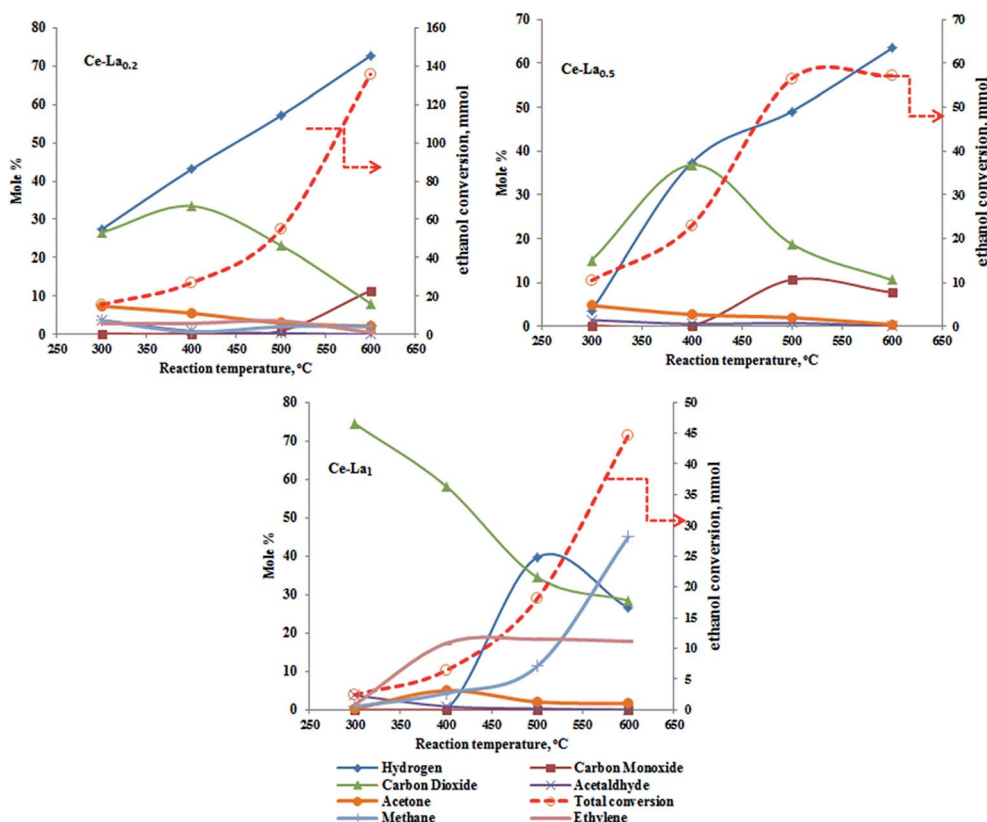

Fig. 14 product distribution during ESR over Ce–La$_x$ catalysts.

H_2/CO_2 ratios (Fig. 15) suggest that the reaction that takes place over Ce–La$_{0.2}$ and Ce–La$_{0.5}$ is indeed ethanol steam reforming reaction (reaction 1), because the experimental values are approximately close to the theoretical ones (≈ 3). The high H_2/CO_2 value in addition to the appearance of CH_4 and CO at reaction temperatures >500 °C indicate that the ethanol decomposition and the reverse WGS reaction ($CO + H_2O \leftrightarrow CO_2 + H_2$) were also taking place at higher reaction temperatures. However, over Ce–La$_1$ catalyst, H_2/CO_2 is $\lll 3$, which indicates that the ESR reaction does not occur completely over this catalyst. The large amount of CO_2, CH_4, acetone and

acetaldehyde (produced in large amounts in the liquid product, not shown here) at reaction temperatures lower than 500 °C indicate the predomination of reactions that lead to acetone ($2C_2H_5OH + H_2O \rightarrow CH_3COCH_3 + CO_2 + 4H_2$) and acetaldehyde ($CH_3CH_2OH \rightarrow CH_3CHO + H_2$) formation, in addition to the methanation reaction ($CO + 3H_2 \rightarrow CH_4 + H_2O$), which was confirmed by the absence of H_2 and CO. Moreover, at reaction temperatures >500 °C, acetaldehyde steam reforming ($CH_3CHO + 3H_2O \rightarrow 5H_2 + 2CO_2$) and its decomposition ($CH_3CHO \rightarrow CH_4 + CO$) were favorable to produce H_2, CO_2, CH_4 and CO. The CO product was consumed in the methanation reaction, which
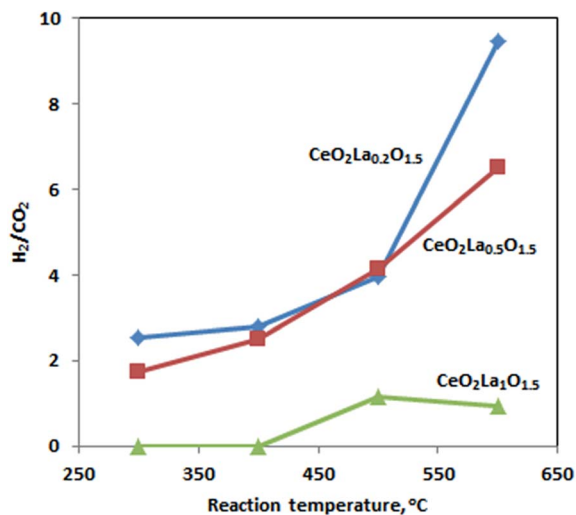
Fig. 15 H_2/CO_2 ratios during ESR over Ce–La$_x$ catalysts.

selectivity to CO_2 and CH_4 slightly increased with time, maybe owing to the gasification of the deposited carbon. The lower stability of Ce–La$_1$ with respect to the other one can be attributed to the large amount of carbon deposit on its surface because of its high selectivity to acetone and ethylene, and acetone being further polymerized to form coke. This data can be confirmed by the characterization of spent catalysts using TGA, XRD and HRTEM techniques.

TGA results (Fig. 17) reveal that there is a significant decrease in the %C by about 3% (at 250 °C) on the Ce–La$_{0.2}$ catalyst and 5% (at 400 °C) on the Ce–La$_1$ catalyst. The lower burning temperature over the two catalysts is attributed to the highly reactive deposited carbon.[49,50] This also indicates that Ce–La$_x$ catalysts prepared by a spray freeze-drying method can be regenerated at about 400 °C in an oxygen atmosphere to restore its original activity.

XRD profiles of spent catalysts (Fig. 18) show that the solid solution structures are well preserved for all the samples after
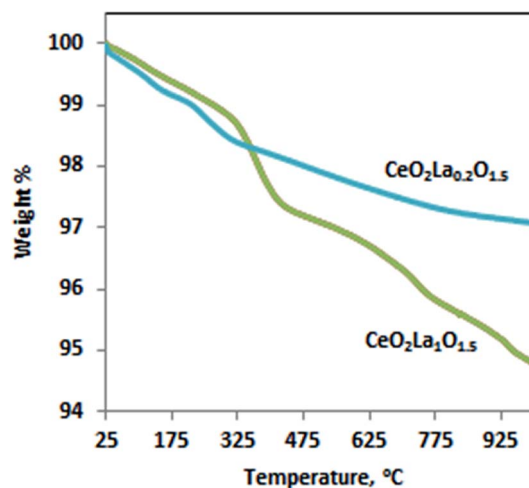
explains the absence of CO and large amounts of CH_4. The very large amounts of CO_2 produced when Ce–La$_1$ is used as a catalyst can be attributed to the large amounts of carbon deposits due to ethanol decomposition, this carbon convert to CO_2 by the effect of La_2O_3. Many authors[46,47] reported that La_2O_3 generates surface oxygen by the formation of $La_2O_2CO_3$ carbonate, which is active for reacting with the surface carbon converting it to CO_2.

Catalytic stability test. To study the effect of the La content on the stability of the prepared catalysts, the ethanol steam reforming reaction was studied over 100 mg Ce–La$_{0.2}$ and Ce–La$_1$ catalysts at 500 °C for 15 h. The Ce–La$_{0.2}$ catalyst was found to be considerably more stable, presenting a more promising behavior than Ce–La$_1$, as shown in Fig. 16. Ce–La$_{0.2}$ catalyst lost only about 0.5% of its activity; the hydrogen selectivity was stable and very high at about 60%, which is close to the theoretical highest selectivity to hydrogen.[48] The selectivity to CO was neglected over the two catalysts and the
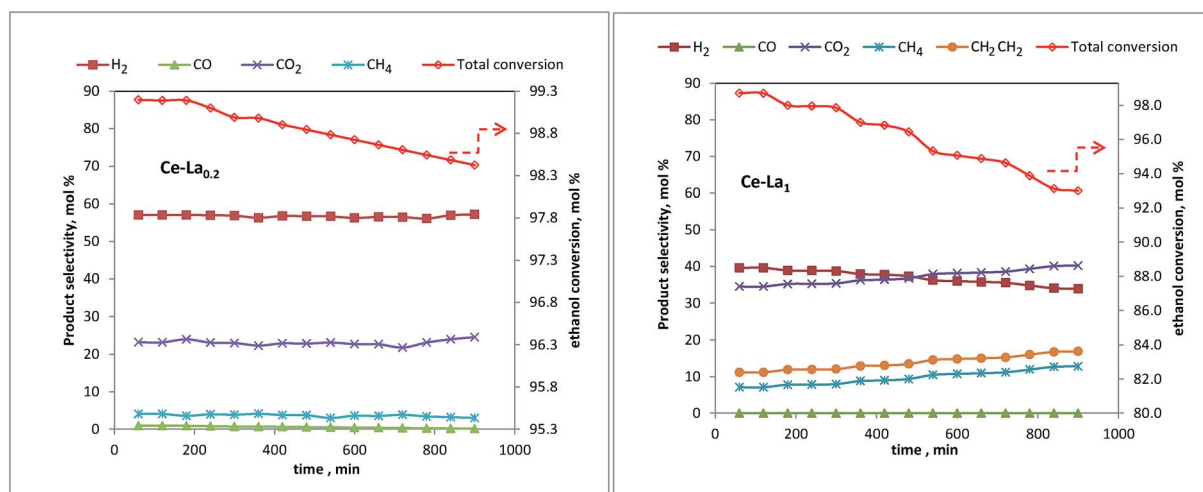

Fig. 17   TGA of spent catalysts.

Fig. 16   Variation of ethanol conversion and product selectivity with reaction time over Ce–La$_{0.2}$ and Ce–La$_1$ catalyst.
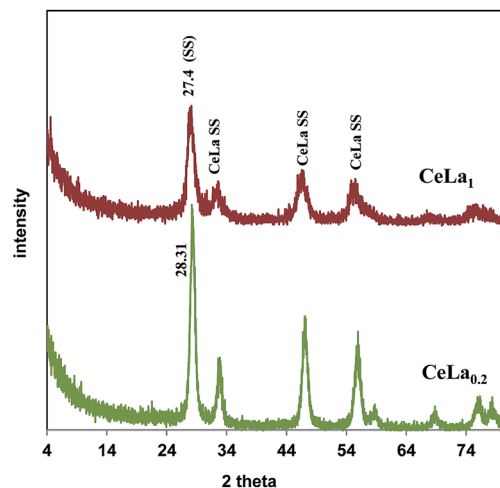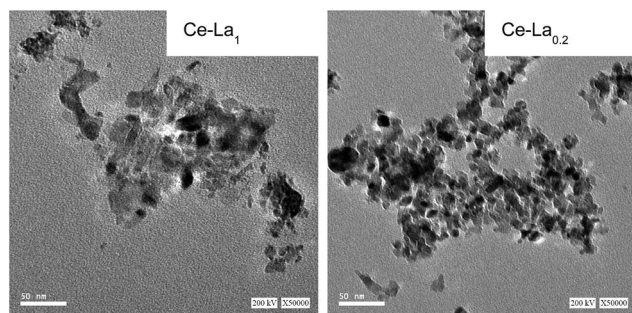
Fig. 18 XRD of spent catalysts.

Fig. 19 HRTEM of spent catalysts.

the stability test (15 h at 500 °C), and the lattice parameter (a) is also found to shift to lower diffraction angles by increasing lanthanum loadings, suggesting that Ce–La$_x$ solid solutions are not affected by the reduction and reaction atmosphere. Moreover, the particle sizes of the used catalysts exhibited very tiny changes (15.65 nm and 54.12 nm for Ce–La$_{0.2}$ and Ce–La$_1$, respectively), indicating that the sintering is neglected during the reaction period. In addition, there are no diffraction peaks due to the deposited carbon, as shown in Fig. 17, which indicates that the deposited carbon was mainly an amorphous one, as shown by TGA data. This was also confirmed by the HRTEM images (Fig. 19), showing that a little amount of amorphous carbon was detected after a much more detailed and meticulous analysis.

4. Conclusion

Ce–La$_x$ catalysts with different La contents ($x = 0.2$, 0.5 and 1) were prepared by spray freeze-drying method. It was found that this method is an excellent one to prepare nano-materials with good characteristic properties, which could be used as a promising catalyst for hydrogen production from ethanol *via* steam reforming reaction. The catalyst showed high ethanol conversion, high hydrogen yield with very low CO selectivity and high stability with very low carbon deposition.

When considering the high hydrogen production with low CO, less than 1%, to be used in a fuel cell, Ce–La$_{0.2}$ was found to be the most selective catalyst, giving 57% H$_2$ and 0.92% CO at a reaction temperature of 500 °C. Studying the effect of La content on the stability of the catalysts reveals that an increase in the La content decreases the catalyst stability to a small extent. The characterizations of the used catalysts show that the deactivation process is attributed to the carbon deposited, and not to the sintering of the catalysts. Moreover, it reveals that the deposited carbon is an amorphous one. Thus, we can regenerate the catalysts to restore its catalytic activity by burning the carbon deposit at about 400 °C in oxygen atmosphere.

References

1 IPCC, *Climate change 2007: mitigation of climate change: contribution of working group III to the fourth assessment report*, Cambridge University Press, U.K., 2007.
2 IEA, energy balances of OECD countries (2006 edition) and energy balances of Non-OECD countries (2006 edition).
3 T. H. Ortmeyer and P. Pillay, Trends in transportation sector technology energy use and greenhouse gas emissions, *Proc. IEEE*, 2001, **89**(12), 1837.
4 V. Nichele, M. Signoretto, F. Menegazzo, I. Rossetti and G. Cruciani, *Int. J. Hydrogen Energy*, 2014, **39**, 4252.
5 E. Kirtay, *Energy Convers. Manage.*, 2011, **52**, 1778.
6 X. Han, Y. Yu, H. He and W. Shan, *Int. J. Hydrogen Energy*, 2013, **38**, 10293.
7 R. M. Navarro, P. MA and F. JLG, *Chem Rev.*, 2007, **107**, 3952.
8 J. Goldemberg, *Science*, 2007, **315**, 808.
9 K. L. Hohn and Y.-C. Lin, *ChemSusChem*, 2009, **2**, 927.
10 L. V. Mattos, G. Jacobs, B. H. Davis and F. B. Noronha, *Chem. Rev.*, 2012, **112**, 4094.
11 M. Ni, D. Y. C. Leung and M. K. H. Leung, *Int. J. Hydrogen Energy*, 2007, **32**, 3238.
12 C. C. Hung, S. L. Chen, Y. K. Liao, C. H. Chen and J. H. Wang, *Int. J. Hydrogen Energy*, 2012, **37**, 4955.
13 L. Chen, C. K. S. Choong, Z. Zhong, L. Huang, T. P. Ang, L. Hong, *et al.*, *J. Catal.*, 2010, **276**, 197.
14 L. V. Mattos, G. Jacobs, B. H. Davis and F. B. Noronha, *Chem. Rev.*, 2012, **112**, 4094.
15 J. D. Holladay, J. Hu, D. L. King and Y. Wang, *Catal. Today*, 2009, **139**, 244.
16 R. A. Elsalamony, D. R. Abd El-Hafiz, M. A. Ebiad, A. M. Mansourb and L. S. Mohameda, *RSC Adv.*, 2013, **3**, 23791.
17 L. Pino, A. Vita, F. Cipitì, M. Laganà and V. Recupero, *Appl. Catal., B*, 2011, **104**, 64.

18 B. M. Reddy, G. Thrimurthulu and L. Katta, *Catal. Lett.*, 2011, **141**, 572.

19 A. Joulia, M. Vardelle and S. Rossignol, *J. Eur. Ceram. Soc.*, 2013, **33**, 2633.

20 M. Hirano, Y. Fukuda, H. Iwata, Y. Hotta and M. Inagaki, *J. Am. Ceram. Soc.*, 2000, **83**, 1287.

21 M. A. Ebiad, D. R. Abd El-Hafiz, R. A. Elsalamony and L. S. Mohamed, *RSC Adv.*, 2012, **2**, 8145.

22 W. P. Hsu, L. Ronnquist and E. Matijevic, *Langmuir*, 1988, **4**, 31.

23 Y. Zhow, R. J. Philips and J. A. Switzer, *J. Am. Ceram. Soc.*, 1995, **78**, 981.

24 E. Tani, M. Yoshimura and S. Somiya, *J. Mater. Sci. Lett.*, 1982, **1**, 461.

25 D. Vie, E. Martnez and F. Sapin, *J. Chem. Mater.*, 2004, **6**, 1697.

26 H. Z. Zhao, S. Ge, X. Zhang, M. Qing, H. Z. Wang and W. J. Zhang, *Refract*, 2005, **39**, 16821.

27 L. X. Li, J. H. Dong and R. Lee, *J. Colloid Interface Sci.*, 2004, **273**, 540.

28 X. Xi, Z. Nie, Y. Jiang, X. Xu and T. Zuo, *Powder Technol.*, 2009, **191**, 107.

29 X. L. Xi, Z. R. Nie, J. C. Yang, X. T. Fu, W. Wang and Y. T. Zuo, *Mater. Sci. Eng., A*, 2005, **394**, 360.

30 X. L. Xi, Z. R. Nie and J. C. Yang, *Appl. Surf. Sci.*, 2005, **251**, 134.

31 L. L. Zhai, X. L. Xi, Z. R. Nie, Y. B. Jang and P. Y. Tong, *Powder Metallurgy Industry*, 2006, **16**, 10.

32 R. A. Elsalamony, D. R. Abd El-Hafiz, M. A. Ebiad, A. M. Mansourb and L. S. Mohameda, *RSC Adv.*, 2013, **3**, 23791.

33 M. Ozawa, R. Onoe and H. Kato, *J. Alloys Compd.*, 2006, **408–412**, 556.

34 X. Han, Y. Yu, H. He, J. Zhao and Y. Wang, *J. Power Sources*, 2013, **238**, 57.

35 L. Liu, X. Wang, M. Guo and M. Zhang, *J. Nanosci. Nanotechnol.*, 2011, **11**, 2155.

36 C. Weidenthaler, *Nanoscale*, 2011, **3**, 792.

37 M. F. Wilkes, P. Hyden and A. K. Bhattacharya, *Appl. Surf. Sci.*, 2003, **206**, 12.

38 G. Wei-ping, *et al.*, *Trans. Nonferrous Met. Soc. China*, 2011, **21**, 2671.

39 Y. Zhang, H. Gu, H. Chen, L. Gao, X. Zhu and L. Guo, *Mater. Res. Bull.*, 2009, **44**, 775.

40 L. P. Li, G. S. Li, J. Xiang, R. I. Smith and H. Inomata, *Chem. Mater.*, 2003, **15**, 889.

41 L. Pino, A. Vita, M. Laganà and V. Recupero, *Appl. Catal., B*, 2014, **148–149**, 91.

42 K. C. Petallidou and A. M. Efstathiou, *Appl. Catal., B*, 2013, **140–141**, 333.

43 D. Gómez, M. A. G. García, M. I. Szynkowska, I. Kocemba and J. M. Rynkowski, *Catal. Today*, 2012, **191**, 142.

44 H. Oh and S. Kim, *Aerosol Sci.*, 2007, **38**, 1185.

45 L. V. Mattos, G. Jacobs, B. H. Davis and F. B. Noronha, *Chem. Rev.*, 2012, **112**, 4094.

46 M. El Doukkali, A. Iriondo, P. L. Arias, J. F. Cambra, I. Gandarias and V. L. Barrio, *Int. J. Hydrogen Energy*, 2012, **37**, 8298.

47 B. Valle, A. Remiro, T. A. Andrés, J. Bilbao and A. G. Gayubo, *Int. J. Hydrogen Energy*, 2013, **38**, 1307.

48 Z. Wang, C. Wang, S. Chen and Y. Liu, *Int. J. Hydrogen Energy*, 2014, **xxx**, 1.

49 M. N. Barroso, M. F. Gomez, L. A. Arru and M. C. Abello, *Int. J. Hydrogen Energy*, 2013, **xxx**, 1.

50 T. Ros, A. Van Dillen, J. Geus and D. Koningsberger, *Chem.–Eur. J.*, 2002, **8**, 1151.